Letter

Strain-tuning of domain walls in multilayer graphene probed in the quantum Hall regime

Paul Anderson,[1,*] Yifan Huang,[2,*] Yuanjun Fan,[2] Sara Qubbaj,[1] Sinisa Coh,[3,†]
Qin Zhou,[2,†] and Claudia Ojeda-Aristizabal[1,†]

[1]*Department of Physics and Astronomy, California State University Long Beach, Long Beach, California 90840, USA*
[2]*Department of Mechanical and Materials Engineering, University of Nebraska, Lincoln, Nebraska 68588-0526, USA*
[3]*Department of Mechanical Engineering and Materials Science and Engineering Program, University of California Riverside, Riverside, California 92521, USA*

(Received 22 March 2021; revised 24 January 2022; accepted 25 January 2022; published 14 February 2022)

Domain walls, topological defects that define the frontier between regions of different stacking order in multilayer graphene, have proved to host exciting physics. The ability to tune these topological defects *in situ* in an electronic transport experiment brings a wealth of possibilities in terms of fundamental understanding of domain walls as well as for electronic applications. Here, we demonstrate, through a MEMS (microelectromechanical system) actuator and magnetoresistance measurements, the effect of domain walls in multilayer graphene quantum Hall effect. Reversible and controlled uniaxial strain triggers the topological defects, manifested as addtional quantum Hall effect plateaus as well as a discrete and reversible modulation of the current across the device. Our findings are supported by theoretical calculations and constitute indication of the *in situ* tuning of topological defects in multilayer graphene probed through electronic transport, opening the way for the use of reversible topological defects in electronic applications.

DOI: 10.1103/PhysRevB.105.L081408

I. INTRODUCTION

With the emergence of the field of 2D materials, strain has provided an external tunable parameter that leads to exciting physics and applications, from strain-induced gauge fields that result in enormous pseudomagnetic fields in graphene [1,2] to devices capable of detecting fine local deformations [3–5]. A few mechanisms have been proven successful in reversibly tuning strain in layered materials [6,7], leading to measurable effects despite layered materials' typical large stiffness [8,9]. An interesting predicted effect in multilayer graphene under strain is the emergence of domain walls, consequence of the applied tension not being distributed evenly across all the graphene layers [10,11].

Domain walls, also known as partial dislocations, are topological defects found at the borderline between different stacking orders in multilayer graphene and are behind intriguing phenomena. They occur naturally and they are restricted to the basal plane, which imposes an extreme boundary condition that results in confinement [12,13]. Bilayer graphene, being the thinnest material that can host such topological defects, has revealed through transmission electron microscopy (TEM) the dynamics and patterns of these defects that are known to behave as solitons [14]. It has been found that electronic transport along the defects occurs through valley-polarized chiral electrons [15–18]. Additionally, it is known that some configurations of partial dislocations completely block electronic transport across the dislocations while others do not have an effect, providing a possible explanation for the both observed metallic and insulating behavior in bilayer graphene at the Dirac point [19,20].

In general, identifying the effect of topological defects in a conductance measurement is challenging. Electronic devices are usually not compatible with imaging techniques such as TEM, and while it has been demonstrated that topological defects can be identified through near-field infrared nanoscopy [15], simultaneous tuning of the defects and conductance measurements remains out of reach. Additionally, because domain walls are naturally occurring in multilayer graphene, their contribution to electronic transport is usually buried within other effects such as charged impurities and other defects. Here, we use a MEMS (microelectromechanical system) actuator to controllably create uniaxial strain in suspended multilayer graphene (six–seven layers) in a reversible and controlled manner, that in turn modifies the domain wall landscape in the multilayer graphene. Domain walls are dynamically created by uniaxial strain applied to the sample using the MEMS actuator while we simultaneously measure electronic transport at low temperature with an external magnetic field. We observe a strain-induced effect on QHE features, as well as a discrete modulation of the current across the device that we attribute to a strain-induced tuning of topological line defects in the multilayer graphene. Theoretical calculations are presented to contrast our findings.

II. SAMPLE FABRICATION

We started with our unique MEMS chips, for which the top surfaces are polished to extremely flat faces with only a few nanometers of surface topology variation, with no deep trenches or holes in contrast with other methods [21]. Such a

*These authors contributed equally to this work.
†Corresponding authors: Claudia.Ojeda-Aristizabal@csulb.edu; sinisacoh@gmail.com; zhouqin1983@gmail.com

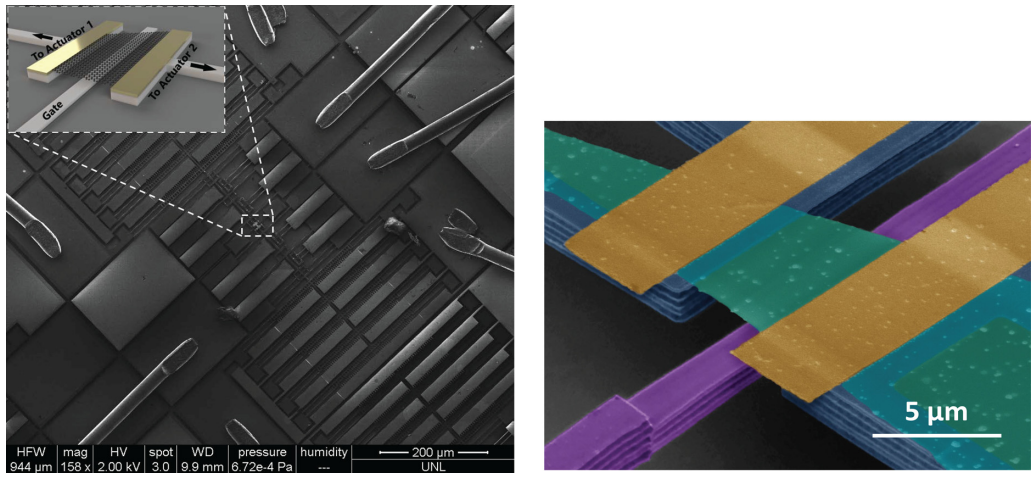

FIG. 1. MEMS actuators and graphene. Left: SEM image of the MEMS chip showing the suspended graphene (represented in the inset) held by movable structural silicon beams connected to the two MEMS actuators. Right: Zoom-in image of the suspended graphene (green) showing source and drain electrodes (yellow) and back gate (purple).

flat surface allows an easy transferring, patterning, and electrical contacting of the multilayer graphene by nanofabrication techniques. Transfer microscopes and micromanipulators allowed us to locate the multilayer graphene and transfer it into precise locations of the MEMS chips. This process is followed by nanolithography to pattern and define clampling metal electrodes and finally, the silicon dioxide sacrificial layer is etched away followed by critical point drying. The integrated six–seven layer graphene is suspended with both ends anchored by metal supports onto a movable structure supported by flexural beams. The metal supports anchor the multilayer graphene sample from its top surface, creating the asymmetry in tension force needed for the creation of domain walls [10,11]. The tension forces are generated by the connected MEMS actuators which utilize electrostatic force. A scanning electron microscopy (SEM) image of the sample is shown in Fig. 1. Detailed fabrication process is described in Appendix A and Supplemental Material [22] (see also Refs. [23–35] therein).

III. ELECTRONIC TRANSPORT MEASUREMENTS AND THEORETICAL CALCULATIONS

Thanks to the fact that MEMS are compatible with high vacuum and cryogenic temperatures, we were able to probe strain-induced effects through electronic transport in a closed cycle cryostat with a superconducting magnet. Electronic transport measurements were performed in a temperature range of 1.5–300 K and magnetic fields up to 12 T on one six–seven layer graphene sample with a close to square geometry. Differential conductance was measured by superimposing an AC voltage (800 μV) to a DC bias voltage (up to 90 mV) and measuring the current modulation by lockin detection. Similarly, differential resistance at zero bias was measured imposing an AC current (10 nA) and measuring the DC voltage drop across the sample.

Despite the fact that domain walls are present in multilayer graphene and do influence electronic transport, their contribution is difficult to discriminate. It is only through the effect of strain and continuous electronic transport measurements that the impact of such defects becomes discernible. Strain was introduced by the electrostatic actuator, where a DC voltage was applied to the MEMS actuators in the range 0–80 V to control the tension on the six–seven layer graphene. This voltage range imposes an averaged strain level of 0–0.21% on the sample, as estimated through the hybrid device model detailed in Appendix B. We observed that the effect of the strain was reversible, reflected both on the sample resistance and on the features of the differential conductance and magnetoresistance, as presented later. Our finite element analysis revealed a nonuniform strain distribution where the strain at the corners of the sample is the highest, where we believe the domain walls are first triggered before traversing the sample (see Supplemental Material [22]). As the inner layers of the multilayer graphene have no contact to the anchors, we believe that strain is applied only to the outermost layers of the six–seven layer graphene. Molecular dynamics (MD) simulations presented elsewhere [36] show that in the case of strained trilayer graphene, interlayer dislocations occur only between the bottom and the middle layers.

Magnetoresistance measurements are presented in Fig. 2. We fixed the actuation voltage and continuously varied the magnetic field as we measured the graphene resistance at zero bias. The data was collected in the following order: $V_{\mathrm{act}} = 80$ V, 0 V, 40 V, 60 V, 20 V. Data for $V_{\mathrm{act}} = 80$ V was very similar to data for $V_{\mathrm{act}} = 60$ V. In the same way, data for $V_{\mathrm{act}} = 0$ V was very similar to $V_{\mathrm{act}} = 20$ V. As will be detailed later, we believe that only $V_{\mathrm{act}} = 40$ V and $V_{\mathrm{act}} = 60$ V imposed a strain on the sample large enough to trigger new domain walls on the sample, discernible in the magnetoresistance measurements. Figure 2 represents only the data for $V_{\mathrm{act}} = 80$ V, $V_{\mathrm{act}} = 40$ V, and $V_{\mathrm{act}} = 0$ V for clarity. A plot of the data for all V_{act} can be found in the Supplemental Material. It can be observed in Fig. 2 an increasing tendency of the quantum Hall effect (QHE) features for larger voltages on the actuators despite the data not being taken in an incremental order for V_{act}. This testifies the reversibility of the strain imposed on the sample. From the data in the

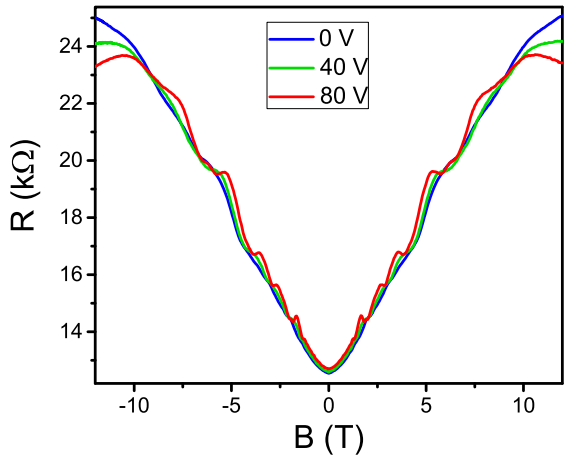

FIG. 2. Magnetoresistance. Experiment and theory. Experimental magnetoresistance at 1.5 K for different voltages on the actuator. 0 V represents no strain and 80 V maximum strain.

absence of strain ($V_{\text{act}} = 0$ V), we deduced the sample mobility $\mu \approx 5000$ cm^2/Vs. This value was extracted from the lowest magnetic field value at which quantum Hall effect features are apparent (2 T), corresponding to a regime where charge carriers complete individual cyclotron orbits before suffering scattering ($\mu B \approx 1$ or $\omega_c \tau \approx 1$). Using values reported in the literature for the effective mass and Fermi velocity in a seven-layer graphene $m^*/m_e = 0.031$ [37] and $v_F = 1.03 \times 10^6$ m/s [38] we estimated a mean free path value of $l_e = 90$ nm, corresponding to a diffusive regime.

Because our measurements are two-probe, quantum Hall effectlike features strongly dependant on the aspect ratio and the geometry of the sample. As reported by Abanin *et al.* [39,40], multilayer graphene samples close to a square geometry ($L \approx W$) present a conductance that is a monotonic function of the filling factor ν with marked QHE plateaus, consistent with the data for our close to square sample ($L/W = 0.7$). Despite the fact that our devices lacked an electrostatic gate which precluded the tuning of the filling factor through the electronic density ($\nu = nh/Be$), the equivalent effect was achieved by varying the magnetic field. As strain was imposed on the sample, features appeared at magnetic fields where QHE plateaus can be identified in the absence of strain. Our data is in qualitative agreement with the outcome of our calculations that we develop next.

We simulated numerically the effect of a domain wall in bilayer graphene QHE, finding QHE plateaus that are absent if no domain walls are included. We consider a 1D domain wall on the plane of a bilayer graphene, perpendicular to the electron flow and subject to a magnetic field perpendicular to the plane of the sample. In general, bilayer graphene is known to present an unconventional QHE, a consequence of the coupling of the two graphene layers that turns graphene's Dirac fermions into chiral quasiparticles with a quadratic dispersion relation, resulting in a characteristic Landau quantization. Figure 3 shows a schematic of the conventional integer QHE typical of a bilayer graphene. The transverse resistivity shows a plateau every time there is a filled integer number of Landau levels, determined by the filling factor $\nu = nh/eB$, with n the electronic density and h Planck's constant. In the bilayer graphene this corresponds to $\nu = nh/eB = 4(N+1)$ with $N = 0, 1, 2, 3, \ldots$. The transverse resistivity takes the form $\rho = (1/(N+1))(4h/e^2)$ with $N = 0, 1, 2, 3, \ldots$ corresponding to $\rho = (1/4)(h/e^2)$, $(1/8)(h/e^2)$, $(1/12)(h/e^2)$, $(1/16)(h/e^2)$, etc. Interestingly, when a domain wall is added perpendicular to the electron flow, additional plateaus appear at $\rho = (1/6)(h/e^2), (1/10)(h/e^2), (1/14)(h/e^2), \ldots$ as shown in Fig. 3 and consistent with another recent theoretical work [41].

The appearance of the additional plateaus can be understood from symmetry arguments. It has been demonstrated in the past that QHE in twisted bilayer graphene presents the same plateau resistance values as a commensurate Bernal bilayer, a consequence of an absence of symmetry breaking [42,43]. Here, the addition of a domain wall creates a sublattice symmetry breaking. Across the domain wall, the A and B carbon sites change places. That is, the carbon atoms that used to be A sites on one side of the domain wall become

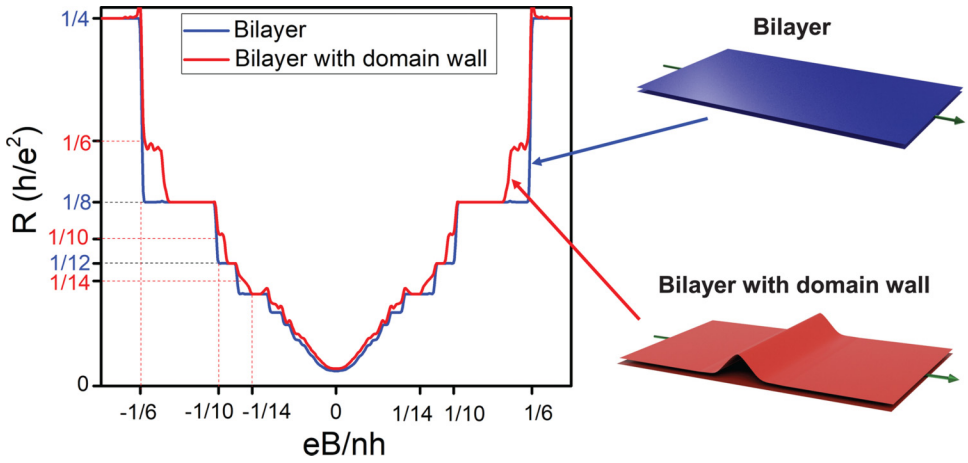

FIG. 3. Quantum Hall resistance in bilayer graphene is contrasted with the effect of adding a domain wall orthogonal to the electron transport. Bilayer QHE plateaus are indicated in black. Additional plateaus appear at $(1/6)(h/e^2)$, $(1/10)(h/e^2)$, $(1/14)(h/e^2)$, …, marked in red. Disorder has been included in the calculations as detailed in Appendix C.

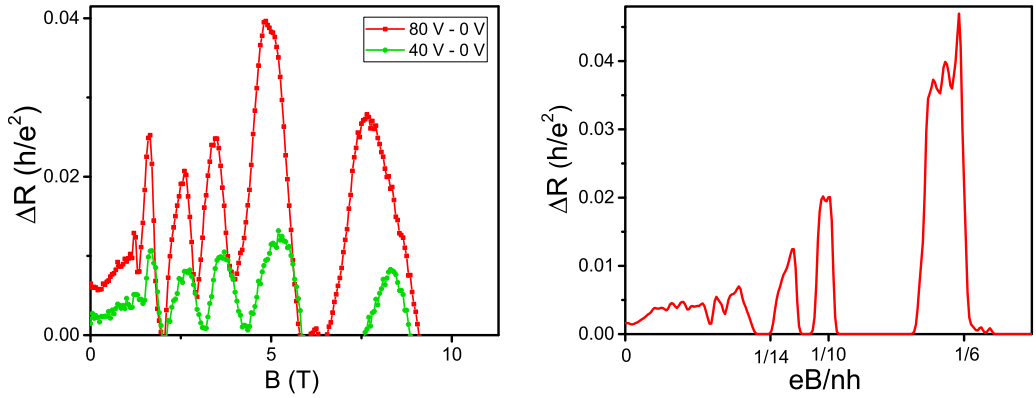

FIG. 4. Magnetoresistance with no domain walls subtracted from the magnetoresistance with domain walls ΔR The experimental ΔR (left) represents the magnetoresistance for a nonzero voltage on the actuator V_{Act} subtracted from the magnetoresistance at $V_{Act} = 0$. The red (green) curve corresponds to the magnetoresistance for $V_{Act} = 80$ V ($V_{Act} = 40$ V) subtracted from the magnetoresistance at $V_{Act} = 0$ V (as represented in Fig. 2). The theoretically calculated ΔR (right) represents the magnetoresistance with a domain wall subtracted from the magnetoresistance with no domain wall, as shown in Fig. 3.

B sites on the other side of the domain wall. Therefore, the A-B sublattice symmetry that prevents midplateaus in bilayer graphene (or two layers of a multilayer graphene) is broken once a domain wall is introduced, giving rise to midplateaus in the transverse resistivity.

We repeated the calculation for six layers of graphene, presented in the Supplemental Material [22]. We found agreement with previous calculations for the transverse resistance of a six-layer graphene [24] $R = (1/(N+3))(4h/e^2)$ with $N = 0, 1, 2, 3, \ldots$ corresponding to $R = (1/12)(h/e^2)$, $(1/16)(h/e^2)$, $(1/20)(h/e^2)$, etc. Plateaus have the same resistivities as those for bilayer graphene, except that the first two plateaus are shifted. Adding a domain wall introduces additional plateaus (in bold) $R = (1/12)(h/e^2)$, $(\mathbf{1/14})(h/e^2)$, $(1/16)(h/e^2)$, $(\mathbf{1/18})(h/e^2)$, $(1/20)(h/e^2)$, $(\mathbf{1/22})(h/e^2)$, $(1/24)(h/e^2)$. This is qualitatively the same as what happens in bilayer graphene, where the plateaus in the presence of a soliton take the values (in bold the plateaus added due to the domain wall) $R = (1/4)(h/e^2)$, $(\mathbf{1/6})(h/e^2)$, $(1/8)(h/e^2)$, $(\mathbf{1/10})(h/e^2)$, $(1/12)(h/e^2)$, $(\mathbf{1/14})(h/e^2)$, $(1/16)(h/e^2)$. While the appearance of midplateaus in the Hall resistivity in the presence of a domain wall seems to be universal, the filling factor (eB/nh values) at which they appear needs further study.

Figure 4 shows the computed difference of the calculated magnetoresistance for a bilayer graphene with and without a domain wall ΔR (right panel) compared to the measured magnetoresistance acquired in the presence and absence of strain in the multilayer graphene (left panel). Despite the fact that we are not able to label the Landau levels, a consequence of a nonfunctional gate voltage, we find a qualitative agreement.

We have represented in the Supplemental Material [22] a fan diagram (Landau level index N vs 1/B) of the QHE features observed in the data both in the absence ($V = 0$) and in the presence of strain ($V = 80V$). In both cases, the data fits to a line as expected. Most importantly, the intercept of the fit with the y axis for the data in the presence of strain is shifted by $1/2$ with respect to the data in the absence of strain. This is expected from the integer sequences for the transverse resistance and the Landau level index for multilayer graphene in the absence and presence of a domain wall, as detailed in the Supplemental Material.

We now turn to the differential conductance measurements presented in Fig. 5, where we observe a discrete modulation of the current across the device as a function of strain, in consensus with reported findings using a different experimental technique. Schweizer *et al.* [44] have demonstrated, through a dedicated scanning electron microscope setup, that partial dislocations in bilayer graphene can be manipulated to turn the sample into different topological states as a result of recombination of the dislocation lines. By using a micromanipulator with a fine tip *in situ*, they create a switching reaction that enables the connection and separation of spatially confined areas of different stacking order that behave as topological switches, where current traveling from source to drain may encounter (or not) areas of different stacking order. We attribute the observed discrete changes of the differential conductance in our samples to be a consequence of a similar effect created by strain, as we develop next.

Differential conductance measurements were taken in the following order: (1) We applied different driving voltages to the MEMS actuators to tension the sample to different strain levels, (2) at each fixed driving voltage, we applied different magnetic fields, and (3) at each fixed magnetic field, we performed differential conductance measurements. (See Supplemental Material for the complete set of data). Interestingly, the differential conductance measured for different voltages on the actuators was identical unless a magnetic field was imposed. The effect became observable at around 1.65 T, close to the onset of quantum oscillations, as observed in the magnetoresistance (Fig. 2). As the magnetic field increased, we noticed that the curves divided into three groups: {0 V, 20 V}, {40 V}, and {60 V, 80 V} (see Fig. 5). We believe that the differential conductance with no voltage on the actuators represents a starting configuration of the domain walls in the sample. As shown in Fig. 5, applying 20 V does not impose a strong enough strain to change the domain wall landscape in the sample. Only 40 V and 60 V generate dislocation reactions that result in discrete changes in the conductance across

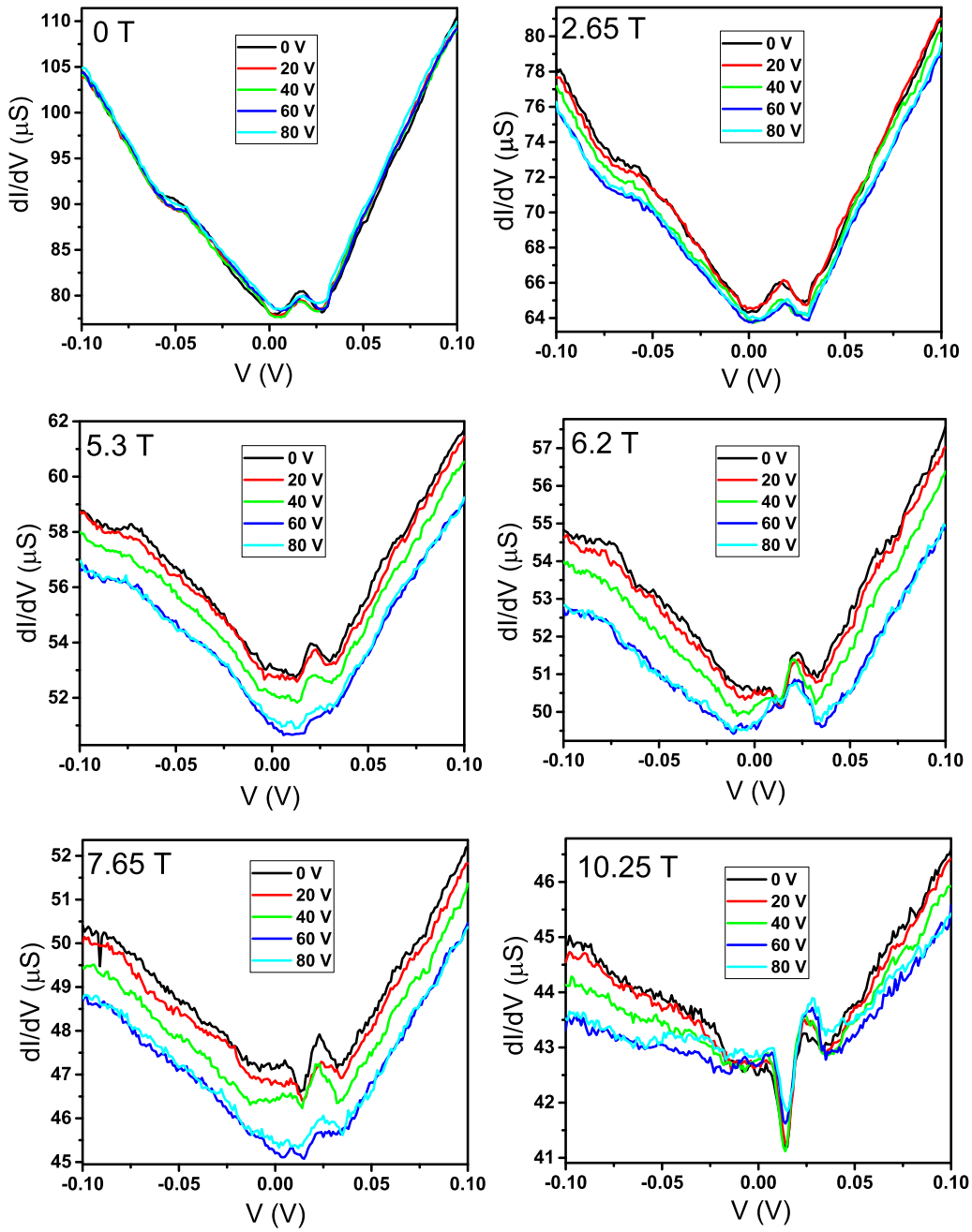

FIG. 5. Differential conductance as a function of the bias voltage for different voltages on the actuator. Each panel shows data taken at different magnetic fields (0 T, 2.65 T, 5.3 T, 6.2 T, 7.65 T, 10.25 T).

the sample. We believe that these changes in the conductance are a consequence of an increase of backscattering, created by the strain-induced domain walls. Indeed, the increment of backscattering is also responsible for the additional QHE plateaus observed with strain (Figs. 2 and 3), as found in our calculations and detailed in Ref. [41].

The overall evolution of the features in the differential conductance near zero bias at different magnetic fields is dictated by the behavior in the absence of strain (see Fig. 6) showing that the domain walls generated by strain have little effect on the phonon modes of the suspended multilayer graphene. As detailed in the Supplemental Material [22], we have found that in the absence of strain and magnetic field, the differential conductance shows features with a periodicity of ≈20 meV (inset of Fig. 6) indicating a coupling to the lowest energy optical phonon mode in graphite, corresponding to neighboring nonequivalent planes vibrating in phase opposition along the *c* axis. A similar behavior for suspended multilayer graphene has been reported in Refs. [28,33].

IV. CONCLUSIONS

Through a reversible and controlled adjustment of uniaxial strain, we were able to tune the electronic transport in

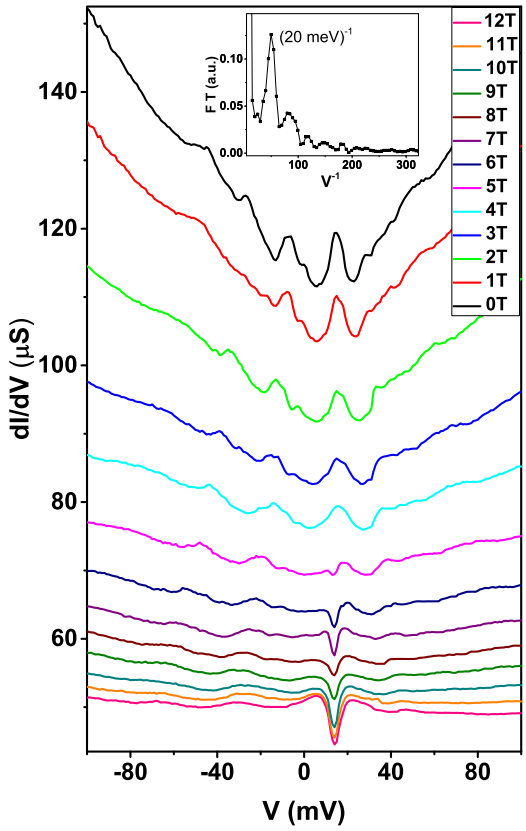

FIG. 6. Bias dependent differential conductance (dI/dV) with no strain at different magnetic fields. Range of 0 T to 12 T. Inset: Fourier transform of the dI/dV at 0T that indicates a periodicity of $(20\ \text{meV})^{-1}$.

suspended graphene, manifested as additional QHE plateaus as well as a discrete modulation of the conductance across the device, consistent with the idea that strain creates domain walls perpendicular to the electron flow and supported by our calculations. In the absence of strain, we identified features in the differential conductance corresponding to the coupling of an optical phonon mode in graphite, in agreement with previous works on suspended multilayer graphene. As strain was applied to the sample, we observed a discrete modulation of the differential conductance across the sample activated by strain that we understand as the tuning of the dislocation landscape in the sample that generates additional scattering when a new domain wall is created across the path of the electrical current.

Most importantly, our results suggest that while adding regular disorder to multilayer graphene preserves its characteristic QHE features, it is only through the addition of domain walls that the quantization of the resistivity is modified. Our work constitutes an experimental illustration of the effect of the arrangement of multilayer graphene domain walls in the quantum Hall effect regime, and it paves the way for the use of reversible topological defects for electronic applications.

ACKNOWLEDGMENTS

The main funding for this work was provided by the U.S. Department of Energy, Office of Science, Office of Basic Energy Sciences under Contract No. DE-SC0018154. S.C. is supported by the National Science Foundation under Grant No. (DMR-1848074). Sample fabrication was partially performed at the Nebraska Nanoscale Facility: National Nanotechnology Coordinated Infrastructure and the Nebraska Center for Materials and Nanoscience, which are supported by the National Science Foundation under Award ECCS: 1542182, and the Nebraska Research Initiative. C.O.-A. would like to acknowledge invaluable advice from David Warren from Oxford Instruments. We would like to acknowledge discussions with as well as preliminary calculations by Gautam Rai and Stephan Haas.

APPENDIX A: FABRICATION PROCESS OF THE MEMS-GRAPHENE HYBRID DEVICE

The process starts with silicon on insulator (SOI) wafers (see figure in the Supplemental Material [22] illustrating the fabrication steps). The top silicon is first patterned to the designed structures using photolithography and deep reactive ion etching. Sacrificial silicon oxide is then filled in between the spacing of the structural silicon. Chemical-mechanical polishing is used to make a smooth top surface for graphene transferring. Thin graphene flakes are first mechanically exfoliated on a Si/SiO_2 substrate. The flakes with the desired number of layers are identified by their optical contrast and then confirmed by their distinct Raman signatures. Then the target graphene flake is transferred with a polymer support by a micromanipulator to a designated location of MEMS chips with high accuracy. Subsequently standard electron-beam lithography techniques are used to pattern graphene and define clamping metal electrodes. In the final step, the silicon dioxide sacrificial filler is etched away in 5:1 BHF, and the chips are dried with a critical point drier to acquire freestanding MEMS devices. In the resulting device, the multilayer graphene is suspended together with the structural silicon beams, because the silicon dioxide beneath has been fully etched away. The movable structural silicon beams are connected to two microactuators that can pull the graphene sample from both ends to opposite directions, controlling the displacement of the graphene.

APPENDIX B: MECHANICAL MODELING

The MEMS-graphene hybrid device consists of two comb-shaped electrostatic actuators at both ends pulling the graphene flake in the middle to opposite directions. We use a lumped model to estimate the displacement of the graphene due to the actuators. At 20 V, 40 V, 60 V, and 80 V, the strain of the graphene flake is estimated as 0.01%, 0.05%, 0.12%, and 0.21%, respectively. See Supplemental Material for details [22].

APPENDIX C: THEORETICAL CALCULATIONS

We computed the quantum transport through the bilayer graphene with a domain wall using the open-source computer package Kwant [45]. For that purpose we considered the bilayer graphene of the finite width of 12 nm. This width is large

enough to eliminate finite-size effects. The scattering region of the bilayer graphene has a length of 7.3 nm. On each side of the bilayer graphene, the scattering region is connected to semi-infinite leads. The tight-binding model for graphene is based on Slater-Koster parametrization from Ref. [46]. Since Slater-Koster parametrization depends only on distances and angles between atoms, we can apply the same parametrization both to the region away from the domain wall or the region near the domain wall. We applied the magnetic field to the model by using the Peierls substitution. The domain wall was modeled by shifting one of the layers of graphene by a fraction of a unit-cell vector so that on each side of the scattering region there is a continuous transition into the semi-infinite leads. The domain wall is modeled with a sigmoid function $\frac{1}{e^{x/a}+1}$ where x is location along the bilayer and parameter a equals 0.8 nm. However, we tested that a larger domain wall size gives qualitatively the same final result for transport. The disorder was modeled by adding a constant onsite energy shift to every carbon site. In the experiment, such an energy shift can be associated to thermal fluctuations or curvature of the sample. The energy shift was chosen at random from a Gaussian distribution with a full width at half maximum of 0.3 eV. Transport was computed and averaged over ten realizations of the disorder. Results using full width at half maximum of 0.1 eV and 0.6 eV gave similar results. For all disorder considered, the quantum Hall effect (QHE) plateaus (associated to a domain wall added perpendicular to the electron flow) were robust and did not disappear as disorder was increased. Disorder widens the QHE plateaus but does not create steps between the plateaus.

[1] F. Guinea, M. Katsnelson, and A. Geim, Energy gaps and a zero-field quantum hall effect in graphene by strain engineering, Nat. Phys. **6**, 30 (2010).

[2] N. Levy, S. Burke, K. Meaker, M. Panlasigui, A. Zettl, F. Guinea, A. C. Neto, and M. F. Crommie, Strain-induced pseudo–magnetic fields greater than 300 tesla in graphene nanobubbles, Science **329**, 544 (2010).

[3] A. Sakhaee-Pour, M. Ahmadian, and A. Vafai, Potential application of single-layered graphene sheet as strain sensor, Solid State Commun. **147**, 336 (2008).

[4] S. B. Kumar and J. Guo, Strain-induced conductance modulation in graphene grain boundary, Nano Lett. **12**, 1362 (2012).

[5] Y. Wang, L. Wang, T. Yang, X. Li, X. Zang, M. Zhu, K. Wang, D. Wu, and H. Zhu, Wearable and highly sensitive graphene strain sensors for human motion monitoring, Adv. Funct. Mater. **24**, 4666 (2014).

[6] H. H. Pérez Garza, E. W. Kievit, G. F. Schneider, and U. Staufer, Controlled, reversible, and nondestructive generation of uniaxial extreme strains in graphene, Nano Lett. **14**, 4107 (2014).

[7] J. H. Hinnefeld, S. T. Gill, S. Zhu, W. J. Swanson, T. Li, and N. Mason, Reversible Mechanical and Electrical Properties of Ripped Graphene, Phys. Rev. Appl. **3**, 014010 (2015).

[8] C. Lee, X. Wei, J. W. Kysar, and J. Hone, Measurement of the elastic properties and intrinsic strength of monolayer graphene, Science **321**, 385 (2008).

[9] S. Bertolazzi, J. Brivio, and A. Kis, Stretching and breaking of ultrathin mos2, ACS Nano **5**, 9703 (2011).

[10] H. Kumar, L. Dong, and V. B. Shenoy, Limits of coherency and strain transfer in flexible 2d van der waals heterostructures: formation of strain solitons and interlayer debonding, Sci. Rep. **6**, 1 (2016).

[11] L. Yang, H. Xu, K. Liu, D. Gao, Y. Huang, Q. Zhou, and Z. Wu, Molecular dynamics simulation on the formation and development of interlayer dislocations in bilayer graphene, Nanotechnology **31**, 125704 (2020).

[12] S. Amelinckx and P. Delavignette, Observation of dislocations in non-metallic layer structures, Nature (London) **185**, 603 (1960).

[13] B. Butz, C. Dolle, F. Niekiel, K. Weber, D. Waldmann, H. B. Weber, B. Meyer, and E. Spiecker, Dislocations in bilayer graphene, Nature (London) **505**, 533 (2014).

[14] J. S. Alden, A. W. Tsen, P. Y. Huang, R. Hovden, L. Brown, J. Park, D. A. Muller, and P. L. McEuen, Strain solitons and topological defects in bilayer graphene, Proc. Natl. Acad. Sci. USA **110**, 11256 (2013).

[15] L. Ju, Z. Shi, N. Nair, Y. Lv, C. Jin, J. Velasco, C. Ojeda-Aristizabal, H. A. Bechtel, M. C. Martin, A. Zettl *et al.*, Topological valley transport at bilayer graphene domain walls, Nature (London) **520**, 650 (2015).

[16] I. Martin, Y. M. Blanter, and A. F. Morpurgo, Topological Confinement in Bilayer Graphene, Phys. Rev. Lett. **100**, 036804 (2008).

[17] F. Zhang, A. H. MacDonald, and E. J. Mele, Valley chern numbers and boundary modes in gapped bilayer graphene, Proc. Natl. Acad. Sci. USA **110**, 10546 (2013).

[18] A. Vaezi, Y. Liang, D. H. Ngai, L. Yang, and E.-A. Kim, Topological Edge States at a Tilt Boundary in Gated Multilayer Graphene, Phys. Rev. X **3**, 021018 (2013).

[19] P. San-Jose, R. Gorbachev, A. Geim, K. Novoselov, and F. Guinea, Stacking boundaries and transport in bilayer graphene, Nano Lett. **14**, 2052 (2014).

[20] S. Shallcross, S. Sharma, and H. B. Weber, Anomalous Dirac point transport due to extended defects in bilayer graphene, Nat. Commun. **8**, 342 (2017).

[21] R. A. Bernal, A. Aghaei, S. Lee, S. Ryu, K. Sohn, J. Huang, W. Cai, and H. Espinosa, Intrinsic bauschinger effect and recoverable plasticity in pentatwinned silver nanowires tested in tension, Nano Lett. **15**, 139 (2015).

[22] See Supplemental Material at http://link.aps.org/supplemental/10.1103/PhysRevB.105.L081408 for schematics of the device fabrication, details on the mechanical modeling of the MEMS-graphene hybrid device, Raman data of the measured device, a finite element analysis to estimate the strain distribution in the graphene flake, a discussion of the measurements on the suspended multilayer graphene in the absence of strain, and a full set of data for the differential conductance of the multilayer graphene in the presence of strain.

[23] H. Li, J. Wu, X. Huang, G. Lu, J. Yang, X. Lu, Q. Xiong, and H. Zhang, Rapid and reliable thickness identification of two-dimensional nanosheets using optical microscopy, ACS Nano **7**, 10344 (2013).

[24] H. Min and A. H. MacDonald, Chiral decomposition in the electronic structure of graphene multilayers, Phys. Rev. B **77**, 155416 (2008).

[25] Y. Cao, V. Fatemi, S. Fang, K. Watanabe, T. Taniguchi, E. Kaxiras, and P. Jarillo-Herrero, Unconventional superconductivity in magic-angle graphene superlattices, Nature (London) **556**, 43.

[26] A. C. Neto, F. Guinea, N. M. Peres, K. S. Novoselov, and A. K. Geim, The electronic properties of graphene, Rev. Mod. Phys. **81**, 109 (2009).

[27] G.-L. Ingold and Y. V. Nazarov, Charge tunneling rates in ultrasmall junctions, in *Single Charge Tunneling* (Springer, Boston, MA, 1992), pp. 21–107.

[28] A. Chepelianskii, P. Delplace, A. Shailos, A. Kasumov, R. Deblock, M. Monteverde, C. Ojeda-Aristizabal, M. Ferrier, S. Guéron, and H. Bouchiat, Phonon-assisted dynamical coulomb blockade in a thin suspended graphite sheet, Phys. Rev. B **79**, 235418 (2009).

[29] A. Bachtold, M. de Jonge, K. Grove-Rasmussen, P. McEuen, M. Buitelaar, and C. Schönenberger, Suppression of Tunneling Into Multiwall Carbon Nanotubes, Phys. Rev. Lett. **87**, 166801 (2001).

[30] M. Bockrath, D. H. Cobden, J. Lu, A. G. Rinzler, R. E. Smalley, L. Balents, and P. L. McEuen, Luttinger-liquid behaviour in carbon nanotubes, Nature (London) **397**, 598 (1999).

[31] B. Altshuler and A. Aronov, Zero bias anomaly in tunnel resistance and electron'electron interaction, Solid State Commun. **88**, 1033 (1993).

[32] Y. Imry and Z. Ovadyahu, Density-of-States Anomalies in a Disordered Conductor: A Tunneling Study, Phys. Rev. Lett. **49**, 841 (1982).

[33] S. Lee, N. Wijesinghe, C. Diaz-Pinto, and H. Peng, Hot electron transport in suspended multilayer graphene, Phys. Rev. B **82**, 045411 (2010).

[34] L. Vitali, M. Schneider, K. Kern, L. Wirtz, and A. Rubio, Phonon and plasmon excitation in inelastic electron tunneling spectroscopy of graphite, Phys. Rev. B **69**, 121414 (2004).

[35] L. Wirtz and A. Rubio, The phonon dispersion of graphite revisited, Solid State Commun. **131**, 141 (2004).

[36] Y. Huang, L. Yang, K. Liu, Z. Wu, and Q. Zhou, Dislocation induced energy dissipation in tunable multilayer graphene resonators, arXiv:2108.11002.

[37] A. Z. AlZahrani and G. P. Srivastava, Graphene to graphite: Electronic changes within DFT calculations, Braz. J. Phys. **39**, 694 (2009).

[38] M. L. Sadowski, G. Martinez, M. Potemski, C. Berger, and W. A. de Heer, Landau level Spectroscopy of Ultrathin Graphite Layers, Phys. Rev. Lett. **97**, 266405 (2006).

[39] D. A. Abanin and L. S. Levitov, Conformal invariance and shape-dependent conductance of graphene samples, Phys. Rev. B **78**, 035416 (2008).

[40] J. R. Williams, D. A. Abanin, L. DiCarlo, L. S. Levitov, and C. M. Marcus, Quantum hall conductance of two-terminal graphene devices, Phys. Rev. B **80**, 045408 (2009).

[41] N. S. Baßler and K. P. Schmidt, Effects of domain walls in bilayer graphene in an external magnetic field, Phys. Rev. B **103**, 155422 (2021).

[42] D. S. Lee, C. Riedl, T. Beringer, A. H. Castro Neto, K. von Klitzing, U. Starke, and J. H. Smet, Quantum Hall Effect in Twisted Bilayer Graphene, Phys. Rev. Lett. **107**, 216602 (2011).

[43] M. Mucha-Kruczyński, I. L. Aleiner, and V. I. Fal'ko, Strained bilayer graphene: Band structure topology and landau level spectrum, Phys. Rev. B **84**, 041404(R) (2011).

[44] P. Schweizer, C. Dolle, and E. Spiecker, In situ manipulation and switching of dislocations in bilayer graphene, Sci. Adv. **4**, eaat4712 (2018).

[45] C. W. Groth, M. Wimmer, A. R. Akhmerov, and X. Waintal, Kwant: a software package for quantum transport, New J. Phys. **16**, 063065 (2014).

[46] G. Trambly de Laissardière, D. Mayou, and L. Magaud, Localization of dirac electrons in rotated graphene bilayers, Nano Lett. **10**, 804 (2010).